Topotactic Intercalation of a Metallic Dense Host Matrix Chalcogenide with Large Electron−Phonon Coupling: Crystal Structures and Electronic Properties of $Li_xMo_2SbS_2$ ($0 \leq x < 0.7$)

Alexandros Lappas,*,† Christopher J. Nuttall,† Zacharias G. Fthenakis,† Vladimir Yu. Pomjakushin,‡ and Mark A. Roberts§

Institute of Electronic Structure and Laser, Foundation for Research and Technology−Hellas, P.O. Box 1527, 711 10 Herakion, Crete, Greece, Laboratory for Neutron Scattering, ETH Zurich & Paul Scherrer Institut, CH-5232 Villigen PSI, Switzerland, and Synchrotron Radiation Source, Daresbury Laboratory, Warrington WA4 4AD, Cheshire, United Kingdom

Received September 16, 2006. Revised Manuscript Received November 1, 2006

The functionality of the three-dimensional ternary chalcogenide Mo_2SbS_2 as a host is demonstrated by low-temperature reactions involving lithium-metal−liquid-ammonia reducing solutions. Rietveld analysis of neutron ($T = 1.5$ and 270 K) and synchrotron X-ray ($T = 300$ K) powder diffraction data proves that topotactic insertion of lithium in quasi-one-dimensional channels produces an isostructural family of $Li_xMo_2SbS_2$ ($0 \leq x < 0.7$) compounds. The optimization of the electronic properties of such a dense host matrix material via intercalation is studied by band structure calculations using the density functional theory (DFT). Mulliken population analysis indicates that a major effect of the presence of Li in the Mo_2SbS_2 is the filling of the d-holes close to Fermi level and therefore only the p-orbitals give rise to mobile carriers in the $Li_xMo_2SbS_2$. Charge disproportionation at the two Mo nonequivalent crystallographic sites and the favorable electrostatic environment of the Li (which is partially depleted of its charge) point to polaron formation, consistent with partial localization upon Li-doping. The resistivity, $\rho(T)$ ($2 \leq T \leq 270$ K), for all compositions studied is modeled by the Bloch−Gruneisen function. Phenomenologically, a percolation model describes the crossover of $\rho(T)$ to a higher conductivity regime at a critical Li composition of $x_c \approx 0.19$. As reflected in the small overall modification to its electronic conductivity, the host efficiently accommodates the perturbations due to chemical and physical ($P \leq 17$ kbar) pressure. The data analysis finds an enhanced electron−phonon coupling constant for Mo_2SbS_2 ($\lambda_t \approx 2.45$) on the basis of the one-electron band-theory model.

1. Introduction

The reductive intercalation of chemically diverse systems with alkali metals has demonstrated that a spectacular transformation of the electronic ground state, from a magnetic insulator to a metal or superconductor, is possible on certain occasions.[1] Valence manipulation by topotactic insertion methods[2] can lead to chemical compounds displaying novel physical behavior. The interplay of structural and electronic properties finds important examples among solids with topologies ranging from zero- (0D)[3] to three-dimensional (3D)[4] lattices. Their capacity for multifunctional capability depends on the host lattice's potential to experience variable perturbations with respect to its crystal chemistry and its electronic properties.

With respect to the latter, there are two categories of hosts,[5] i.e., insulating (e.g., zeolites) and electronically conducting (e.g., graphite). Good host systems adopt a percolation network of vacant sites that can afford reasonable diffusion of suitable size molecules or ions. In particular, layered hosts with relatively high electronic conductivity have been the subject of intensive studies mainly because of their ability to adapt into the guest species.[6] However, other systems with high coordination numbers of the matrix constituent elements together with redox-active transition metals for high electronic conductivity are more scarce hosts. For example, Chevrel phases $M_xMo_{3n}X_{3n+2}$ ($n \geq 2$, M = monovalent main group metal)[7] and chalcogenide spinel $CuCr_2X_4$ compounds[8] with interconnected channels or β-vanadium bronzes β-$A_xV_2O_5$ ($x \approx 1/3$, A = Li, Na, Ag, Ca, Sr, and Pb)[9] with isolated parallel lattice tunnels present

* Corresponding author. E-mail: lappas@iesl.forth.gr.
† Foundation for Research and Technology−Hellas.
‡ Laboratory for Neutron Scattering ETH Zurich & Paul Scherrer Institut.
§ Daresbury Laboratory.

(1) (a) O'Hare, D. in *Inorganic Materials*; Bruce, D. W., O'Hare, D., Eds.; Wiley & Sons: London, 1996; Chapter 4. (b) Friend, R. H.; Yoffe, A. D. *Adv. Phys.* **1987**, *36*, 1.
(2) Schaak, R. E.; Mallouk, T. E. *Chem. Mater.* **2002**, *14*, 1455.
(3) (a) Fleming, R. M.; Ramirez, A. P.; Rosseinsky, M. J.; Murphy, D. W.; Haddon., R. C.; Zahurak, S. M.; Makhija, A. V. *Nature* **1991**, *352*, 787. (b) Rosseinsky, M. J. *J. Mater. Chem.* **1995**, *5*, 1497.
(4) (a) Johnston, D. C.; Prakash, H.; Zachariasen, W. H.; Viswanathan, R. *Mater. Res. Bull.* **1973**, *8*, 777. (b) Harrison, M. R.; Edwards, P. P.; Goodenough, J. B. *Philos. Mag. B* **1985**, *52*, 679.
(5) Schöllhorn, R. *Chem. Mater* **1996**, *8*, 1747.
(6) (a) Rouxel, J. *Rev. Inorg. Chem.* **1979**, *1*, 245. (b) Wu, C.-G.; DeGroot, D. C.; Marcy, H. O.; Schindler, J. L.; Kannewurf, C. R.; Bakas, T.; Papaefthymiou, V.; Hirpo, W.; Yesinowski, J. P.; Liu, Y.-J.; Kanatzidis, M. G. *J. Am. Chem. Soc.* **1995**, *117*, 9229. (c) Yamanaka, S.; Hotehama, K.; Kawaji, H. *Nature* **1998**, *392*, 580.
(7) Chevrel, R.; Sergent, M.; Prigent, J. *J. Solid State Chem.* **1971**, *3*, 515.
(8) Van Stapele, R. P. In *Ferromagnetic Materials: A Handbook on the Properties of Magnetically Ordered Substances*; Wohlfarth., E. P., Ed.; North-Holland: Amsterdam, 1982; Vol. 3, pp 603-745.

10.1021/cm0622147 CCC: $37.00
Published on Web 12/13/2006 PAGE EST: 9.2

structural types that provide diffusion pathways with rather narrow dimensions that would be accessible only to atomic guests. For this reason, low-temperature reduction of existing hosts by alkali metal vapor[10] or solvated electrons[11] is an attractive alternative strategy. Attempts to optimize the properties of such dense host matrix materials highlight the importance of precise control over the oxidation state of constituent atoms.[12]

As part of a search for new crystalline conducting materials via alkali metal insertion reactions, we have examined the effect of the redox Li intercalation on the crystal structure and electronic properties of the recently reported[13] compound Mo_2SbS_2 (a dense host matrix material), which represents a new family of 3D connected, ternary antinomy-chalcogenide structures.[14,15] Redox intercalation generally requires both ionic transport of the guest species and electronic transport in the host lattice. To this end, Li intercalation into Mo_2SbS_2 could be especially interesting electronically because the material has been claimed to exhibit mixed valency and superconductivity.[13] The addition of carriers by intercalation is a promising method for modifying its electronic structure, as doping by intercalation exploits the interstitial crystal sites and therefore a high level of doping is possible without introducing disorder into the host matrix structure. We determined the crystal structures of $Li_xMo_2SbS_2$ ($0 \leq x < 0.7$) by neutron and synchrotron X-ray powder diffraction, measured their transport and magnetic properties at ambient as well as high-pressure, and furthermore studied their electronic band structure on the basis of the density functional theory.

2. Experimental Section

2.1. Lithium Intercalation. In this work, the reductive intercalation chemistry of Mo_2SbS_2 has been investigated through a process involving alkali-metal−liquid-ammonia synthesis. Initially, phase-pure Mo_2SbS_2 samples were prepared in a modified version of a method previously reported.[13] Stoichiometric quantities of Mo (99.99%), newly sublimed S (99.9%), and Sb (99.999%) were ground together and pressed into pellets (∼0.5 g) inside an Ar recirculating, anaerobic glovebox ($O_2 \approx 1$ ppm and $H_2O < 1$ ppm). They were sealed in silica ampoules at $<1 \times 10^{-4}$ mbar and heated to 1050 K for 45 h. Samples were then reground in the glovebox and annealed as free-flowing powders with small quantities of I_2 as a mineralizing agent, for 20 h at 673 K (typically, 40 mg of I_2 was added into a 120 mm long, 10 mm I.D. silica ampule). Prolonged heating resulted in the formation of the impurity phase MoS_2, clearly visible from laboratory X-ray diffraction (XRD) patterns. Subsequently, solvated electrons formed in metal−ammonia solutions were used to partially reduce the Mo_2SbS_2. In a typical intercalation experiment, NH_3(l) (cryogenically distilled over Na(s)) was condensed at −78 °C into an ampule containing Li and Mo_2SbS_2 in a 1:1 molar ratio. After distilling and recondensing the NH_3(l) from the sample a few times over a period of a few hours and while stirring, the characteristic alkali/NH_3(*l*) blue color significantly diminished; the resulting clear solution indicated possible alkali intercalation. Finally, the liquid NH_3 was evaporated, the sample was dried at 473 K under dynamic vacuum ($<1 \times 10^{-4}$ mbar), eliminating any surface-absorbed or co-intercalated NH_3, and the $Li_xMo_2SbS_2$ air-sensitive product was brought into the glovebox for physical property characterization. To investigate the effect of progressive Li intercalation using Li/NH_3 solution, we carried out a set of reactions with nominal Li:Mo_2SbS_2 molar ratios of 0.2:1, 0.4:1, 0.6:1, 0.8:1, and 1.0:1. Specimens sealed in Ø0.5 mm glass capillaries were routinely checked for their crystallinity by X-ray powder diffraction (Rigaku D/MAX-2000H; 12 kW Cu*K*α rotating anode). Similar reactions were also undertaken with Na/NH_3 solutions. However, the low crystallinity of the resulting powders deterred us from further studies in this direction.

2.2. Neutron and Synchrotron X-ray Diffraction. Neutron powder diffraction (NPD) patterns on Mo_2SbS_2 (∼1.96 g) and intercalated $Li_xMo_2SbS_2$ (∼1.9 g; nominal $x = 1.0$) samples placed inside He-filled V-cans (Ø5 mm; sealed with In wire in the glovebox) were recorded on the high-resolution diffractometer HRPT of the SINQ neutron source at the Paul Scherrer Institute, Switzerland. Rietveld refinable (FULLPROF code)[16] powder patterns were collected in the range $5 \leq 2\theta \leq 165°$ at different wavelengths so that either the high-intensity mode ($\lambda = 1.494$ Å) or the high-resolution mode ($\lambda = 1.8856$ Å) could be utilized, with a scan step width of $\Delta 2\theta = 0.1°$. A continuous flow ILL-type, orange cryostat allowed temperatures between 1.5 and 300 K to be studied. $Li_xMo_2SbS_2$ samples with nominal compositions $0 < x \leq 1.0$, sealed in Ø0.5 mm borosilicate glass capillaries, were also investigated at the high-flux 9.1 station of the synchrotron radiation source at the Daresbury Laboratory, United Kingdom. Synchrotron X-ray diffraction data were recorded between $4 \leq 2\theta \leq 61°$ at room temperature ($\lambda = 0.8700$ Å, with step width $\Delta 2\theta = 0.01°$), whereas their Rietveld refinement was carried out with the GSAS[17] suite of programs.

2.3. Electronic Property Measurements. Dc magnetic susceptibility measurements for Mo_2SbS_2 were performed on a Quantum Design MPMS superconducting quantum interference device (SQUID), in an applied magnetic field of 100 G. The temperature dependence ($2 \leq T \leq 300$ K) of the dc electrical resistivity in $Li_xMo_2SbS_2$ series was measured using a conventional four probe technique, based on a homemade setup (see Appendix I in the Supporting Information), allowing both ambient and high-pressure ($P < 2$ GPa) studies.

3. Theoretical Methods

In this work, band structure, and related calculations were carried out using the density functional theory (DFT) in the generalized gradient approximation (GGA) as implemented in the CASTEP code,[18] with the Perdew−Burke−Ernzerhof (PBE)[19] exchange correlation functional (see Appendix IIa in Supporting Information). To find the density of states (DOS) and the band structure of any

(9) Yamada, H.; Ueda, Y. *J. Phys. Soc. Jpn.* **1999**, *68*, 2735.
(10) Zhou, W., Anderson, P. A.; Liu, C.; Edwards, P. P. *Physica C* **1991**, *190*, 59.
(11) Somoano, R. B.; Hadek, V.; Rembaum, A. *J. Chem. Phys.* **1973**, *58*, 697. Anderson, P. A.; Barr, D.; Edwards, P. P. *Angew. Chem., Int. Ed.* **1991**, *30*, 1501.
(12) Schöllhorn, R. In *Progress in Intercalation Research*; Müller-Warmuth, W., Schöllhorn, R., Eds.; Kluwer: Dordrecht, The Netherlands, 1994; p 1.
(13) Lee, C.-S.; Safa-Sefat, A.; Greedan, J. E.; Kleinke, H. *Chem. Mater.* **2003**, *15*, 780.
(14) Kleinke, H. *Chem. Commun.* **2000**, 1941.
(15) Lee, C.-S.; Kleinke, H. *Eur. J. Inorg. Chem.* **2002**, 591.
(16) Rodriguez-Carvajal, J. *Physica B* **1993**, *192*, 55.
(17) Larson, A.; Von Dreele, R. B. *General Structure Analysis System (GSAS)*; Report LAUR 86-748; Los Alamos National Laboratory: Los Alamos, NM, 2004.
(18) Payne, M. C.; Teter, M. P.; Allan, D. C.; Arias, T. A.; Joannopoulos, J. D. *Rev. Mod. Phys.* **1992**, *64*, 1045.
(19) Perdew, J. P.; Burke, K.; Ernzerhof, M. *Phys. Rev. Lett.* **1996**, *77*, 3865.

intercalated $Li_xMo_2SbS_2$ composition, we used an interpolation scheme between the DOS of the Mo_2SbS_2 and the DOS of the $LiMo_2SbS_2$ optimized crystalline structures. Technical aspects of this methodology, concerning solid-solution behavior, are described in Appendix IIb of the Supporting Information. Because CASTEP affords such calculations at a very accurate level, it was used in order to predict the optimum crystal structures (i.e., the atomic positions and unit-cell parameters, which minimize the energy of the crystal) required for the above-mentioned interpolation scheme.

4. Results and Discussion

4.1. Crystal Structure Determination. Within the detection limit (<4% volume) of the conventional laboratory XRD studies, single-phase samples were assumed and all the patterns were indexed on the basis of the earlier room temperature (R.T.) results.[13] For this reason, a similar crystallographic model was employed as a starting point for the low-temperature structure determination of Mo_2SbS_2 by NPD Rietveld refinements; Mo_2SbS_2 samples were found to be phase pure. In addition, no structural phase change was observed from 270 down to 1.5 K. Refinements in space group $P2_1/m$ showed marginal thermal contraction of the monoclinic lattice, i.e., $\Delta a = 0.10(2)\%$, $\Delta b = 0.18(2)\%$, $\Delta c = 0.10(2)\%$. Table 1 compiles the experimental structural parameters.

Full-profile analysis involved the variation of a number of profile and instrumental parameters; the scale factor for each phase involved, the zero point shift, the 12-term cosine Fourier series background function (refined initially and then kept fixed), and the peak shape broadening as modeled by a pseudo-Voigt function, with anisotropy at low scattering angles. The occupancy of each Mo, Sb, and S site was refined but found not to deviate from the stoichiometric values. The corresponding Rietveld refined pattern is shown in Figure 1a and is compared to that obtained from the lithiated material in Figure 1b. The refinement of the $Li_xMo_2SbS_2$ structure at 1.5 K was carried out by combining NPD data (recorded at $\lambda = 1.494$ Å (#1) and $\lambda = 1.8856$ Å (#2)) with that of the parent compound to supply the starting model. Combining the datasets provided increased statistical accuracy to our refinements and allowed us to identify some low-intensity Bragg reflections (e.g., at $2\theta \approx 29.7$, 34.6, 59.1, 59.4, and 61.7°; $\lambda = 1.494$ Å) as impurities that were indexed to a $LiNH_2$ phase.[20] It appears that the "chimie douce" approach followed in our work catalyzed the decomposition of the metastable Li/NH_3 solution to form $LiNH_2$ as a byproduct, an effect that has been observed before in Li intercalates of Ruddlesden−Popper oxysulfides.[21] Two-phase Rietveld analysis found $LiNH_2$ to account for ~3.6% of the total integrated intensity, with an improved quality of fit; i.e., for pattern #1 only, χ^2 developed from 4.31 to 3.32 (R_{wp} from 2.51 to 2.15%).

The Li intercalated in Mo_2SbS_2 was first located by using difference Fourier methods. A starting structural model based on the parent material's low-T structure was Rietveld fitted to the NPD data of the $Li_xMo_2SbS_2$ material. Because all the constituent atoms of the host have been of positive scattering length, using this method with neutrons offers certain advantages as the Li site (scattering length for Li = −1.90 fm) was identified as a large negative intensity peak in the difference Fourier ($F_{obs} - F_{calcd}$) map. Refining the Li site gave the stoichiometry of the intercalate as $Li_{0.31(2)}Mo_2SbS_2$. The quality of fit was considerably improved with the inclusion of Li, namely with $x = 0.31(2)$, $\chi^2 = 2.707$, cf. for $x = 0.0$, $\chi^2 = 3.324$ (χ^2 here is the "global" value, i.e., that for combined datasets), at the 2*e* crystallographic position, 0.612(5), 0.25, 0.144(3). For these purposes, the isotropic thermal parameter for Li was fixed to $B_{iso} = 0.3$ Å^2, the overall Debye−Waller temperature factor of the structure in early stage refinements. The Li cation adopts a pseudo-octahedral coordination of 5-S and 1-Sb nearest neighbors (nn) and resides within the quasi-one-dimensional channels of Mo_2SbS_2 (Figure 2). The final refined atomic coordinates of $Li_{0.31}Mo_2SbS_2$ are given in Table 1, with selected bond distances and angles in Table 2.

Table 1. Fractional Coordinates and Atomic Thermal Displacements from Rietveld Refinement of Neutron Powder Diffraction (NPD) Data for $Li_xMo_2SbS_2$[a]

	Mo_2SbS_2	Mo_2SbS_2	$Li_{0.31(2)}Mo_2SbS_2$
volume fraction (%)	100	100	96.4
T (K)	270	1.5	1.5
scan duration (h)	5	24	16
a (Å)	6.5047(2)	6.4980(2)	6.5783(3)
b (Å)	3.18412(8)	3.17826(8)	3.18122(14)
c (Å)	9.3426(3)	9.3335(3)	9.5356(4)
β (deg)	105.422(2)	105.421(2)	104.893(3)
V (Å^3)	186.535(9)	185.819(8)	192.848(15)
Mo(1)			
x	0.6444(4)	0.6652(3)	0.6651(5)
z	0.4804(3)	0.4805(2)	0.4806(3)
B_{iso} (Å^2)	0.56(4)	0.29(3)	0.22(5)
Mo(2)			
x	0.8927(4)	0.8926(3)	0.8976(5)
z	0.8844(2)	0.8846(2)	0.8802(3)
B_{iso} (Å^2)	0.40(4)	0.23(4)	0.20(6)
S(1)			
x	0.5194(9)	0.5209(9)	0.5248(11)
z	0.6897(7)	0.6901(6)	0.6881(8)
B_{iso} (Å^2)	0.92(9)	0.60(8)	0.30(11)
S(2)			
x	0.2647(8)	0.2650(8)	0.2586(10)
z	0.9870(6)	0.9872(6)	0.9919(7)
B_{iso} (Å^2)	0.70(9)	0.52(8)	0.48(12)
Sb			
x	0.9969(4)	0.9971(4)	1.0056(5)
z	0.3379(3)	0.3376(3)	0.3443(4)
B_{iso} (Å^2)	0.84(5)	0.48(4)	0.35(6)
Li			
x			0.612(5)
z			0.144(3)
#1 R_{wp} (%), R_p (%)	4.13, 3.29	2.82, 2.18	2.15, 1.67
#2 R_{wp} (%), R_p (%)			2.97, 2.33
#1 χ^2, 2θ (deg)	1.47, 8.5−165	3.63, 8.5−165	3.32, 8−165
#2 χ^2, 2θ (deg)			2.11, 10.5−165
#1 $N-P+C$, P, R	3087, 38, 547	1525, 38, 544	1498, 70, 570
#2 $N-P+C$, P, R			1473, 70, 293

[a] Two combined datasets at $\lambda = 1.494$ Å (#1) and $\lambda = 1.8856$ Å (#2) were used for the analysis of the $Li_{0.31(2)}Mo_2SbS_2$ structure (numbers of N observations, P refined variables, and R independent reflections are given). Space group $P2_1/m$ ($Z = 2$); atoms in the unit cell were refined in positions 2*e* in (*m*): x, 1/4, z.

4.2. Comparative Structural Features. The structure of $Li_xMo_2SbS_2$ (Figure 2) is composed of two primary building blocks: (i) the $[MoSbS]_\infty$ layers of β-$MoTe_2$ topology,[22] where Mo(1) adopts pseudo-octahedral sites (MoS_3Sb_3 units),

(20) Jacobs, H.; Juza, R. *Z. Anorg. Allg. Chem.* **1972**, *391*, 271.
(21) Hyett, G.; Rutt, O. J.; Gai, Z. A.; Denis, S. G.; Hayward, M. A.; Clarke, S. J. *J. Am. Chem. Soc.* **2004**, *126*, 1980.

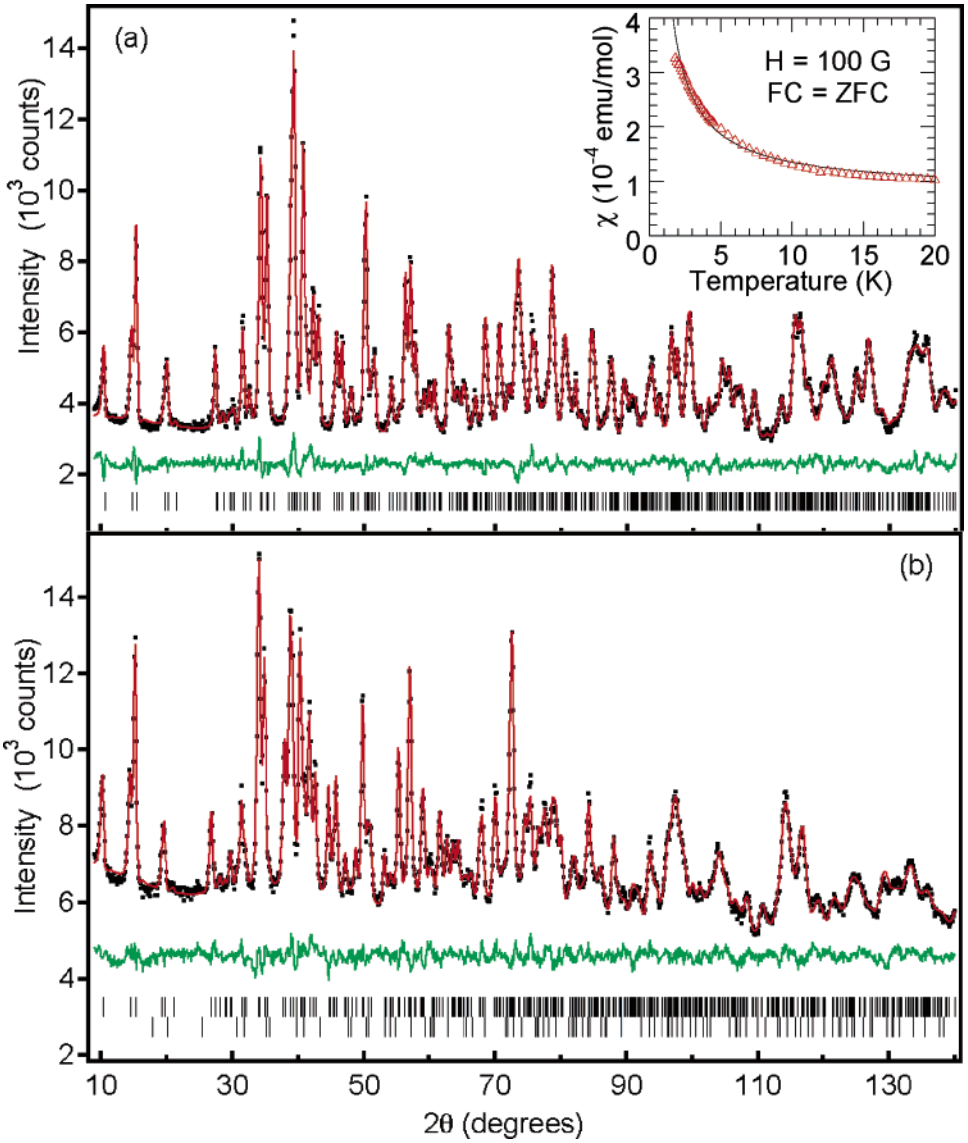

Figure 1. Rietveld refined profiles, observed (black points), calculated (red line), and difference (green line), at $T = 1.5$ K and $\lambda = 1.494$ Å for (a) Mo_2SbS_2 and (b) $Li_{0.31(2)}Mo_2SbS_2$, with the bottom set of tick marks assigned to a $LiNH_2$ impurity. Inset to (a): dc susceptibility of Mo_2SbS_2, fitted to the Curie law.

with a zigzag connectivity along the *b*-axis, and (ii) the $[MoS]_\infty$ zigzag chains, where the Mo(2) type of site (MoS_4Sb_2 units) provides the connectivity to the layers via two Sb and one S(1) atoms. NPD indicates that Li intercalation results in an anisotropic expansion of the Mo_2SbS_2 lattice, largely in the *ac* plane ($\Delta a = 1.24(2)\%$, $\Delta b = 0.10(2)\%$, and $\Delta c = 2.17(2)\%$ at 1.5 K). We note that the interlayer chalcogen−chalcogen separation varies from 3.86 Å in the 2D β-$MoTe_2$ to 5.77 Å and 6.08 Å in the 3D dense host matrix chalocogenides $MoSb_2S$[15] and Mo_2SbS_2, respectively. This corroborates to an interlayer octahedral void space around the 2*e* Li site of the Mo_2SbS_2 unit cell that is effectively larger than that in the topologically related compounds of β-$MoTe_2$ and $MoSb_2S$, all composed of CdI_2-like layers. As such, the host favors intercalation of cations and the new material, $Li_{0.31}Mo_2SbS_2$, has 6.25 Å interlayer S−S separation distances. The effect is best depicted with reference to the bond angles Mo(2)−$\hat{S}$(2)−Mo(2), within the $[MoS]_\infty$ chains and the bond length Mo(2)−S(1), which joins the chains to the $[MoSbS]_\infty$ layers (Figure 2). At 1.5 K, the bonds calculated from NPD are considerably elongated, whereas the angles "open up" from 70.8(2) to 73.3(2)° upon intercalation (Table 2).

Rietveld refinements of the synchrotron X-ray data (300 K) demonstrate that chemical pressure manifests as lattice swelling in the $Li_xMo_2SbS_2$ series, e.g., 186.54(1) Å^3 in $x = 0$ rises to 192.97(1) Å^3 in $x = 0.69(3)$. A representative pattern ($\chi^2 = 6.381$, $R_{wp} = 4.93\%$) is shown in Figure 3 for the maximum attainable lithiated composition ($x = 0.69$). Details of the structure solution and refinement strategy are provided in the Supporting Information (Appendix III), with the crystallographic parameters and bond distances reported in Tables S1 and S2. No deviations from the monoclinic $P2_1/m$ structure were found for all compositions with $x < 0.7$. The variation in the lattice parameters with Li content is shown as the inset to Figure 3. Their composition dependence shows deviations from a simple linear variation expected for an ideal solid solution obeying the so-called

(22) (a) Brown, B. E. *Acta. Crystallogr.* **1966**, *20*, 268. (b) Kertesz, M.; Hoffmann, R. *J. Am. Chem. Soc.* **1984**, *106*, 3453.

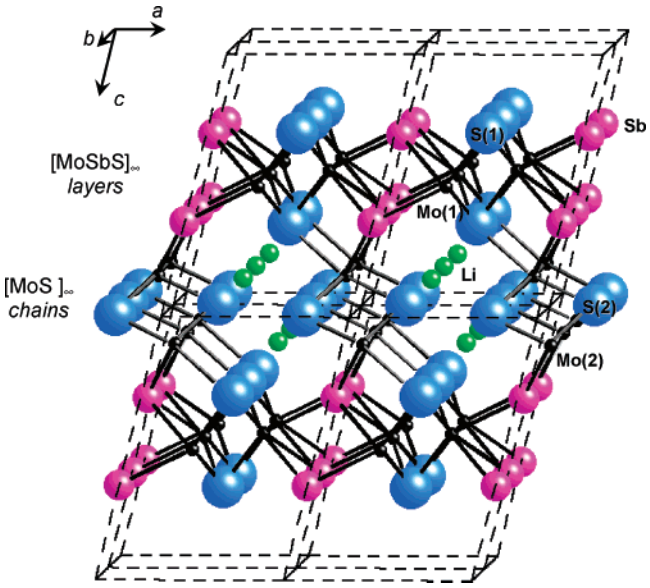

Figure 2. Eight unit cells of the Rietveld refined $Li_{0.31(2)}Mo_2SbS_2$ structure, viewed down the *b*-axis; Mo atoms (black), S atoms (blue), Sb atoms (pink), and Li atoms (green).

Table 2. Selected Bond Lengths (Å) for $Li_xMo_2SbS_2$ Compositions as Derived from Rietveld Refinements of the 1.5 K Neutron Powder Diffraction Data.

		Mo_2SbS_2,1.5 K	$Li_{0.31(2)}Mo_2SbS_2$,1.5 K
Mo(1)	Mo(1)	3.17826(8) × 2	3.1812(1) × 2
		2.772(2) × 2	2.793(4) × 2
	Sb	2.821(4)	2.863(5)
		2.871(2) × 2	2.855(3) × 2
	S(1)	2.384(7)	2.390(9)
		2.345(4) × 2	2.375(5) × 2
Mo(2)	Mo(2)	3.17826(8) × 2	3.1812(1) × 2
		2.741(2) × 2	2.825(3) × 2
	Sb	2.851(3) × 2	2.867(4) × 2
	S(1)	2.607(5)	2.657(7)
	S(2)	2.354(5)	2.339(7)
		2.379(5) × 2	2.392(6) × 2
Sb	Sb	3.17826(8) × 2	3.1812(1) × 2
		3.414(4) × 2	3.386(5) × 2
Li	Mo(1)		3.14(3)
	Mo(2)		3.66(3) × 4
			3.51(3)
	Sb		2.79(3)
	S(1)		2.58(3) × 2
	S(2)		2.34(3) × 2
			2.40(3)

Vegard's law. Such deviations,[23] common in metallic solid solutions, imply strong interaction between electrons or atoms as the doping level increases. Therefore, size effects are not the only reason behind the observed changes, as electronic effects are expected to act in a coordinated way.

Longer bond distances in the vicinity of a matrix transition element will corroborate to a reduced host. The synchrotron data for the $Li_xMo_2SbS_2$ series ($0 \le x < 0.7$) support such a chemical reactivity, as lithiation leads to elongation of Mo bond lengths (see Table S3 in the Supporting Information): Mo(2)−S(1) increases from 2.618(6) to 2.652(4) Å and Mo(2)−Sb increases from 2.855(3) to 2.867(1) Å (Figure 4a). These provide a pathway (Figure 2) for the interplane coupling between the $[MoS]_\infty$ chainlike motifs and the $[MoSbS]_\infty$ layers. For comparison, the "in-chain" bond evolution is reported in Table S3 of the Supporting Information. Concerning the Mo(1)−S(1) connectivity, one long bond of 2.386(8) Å remains unperturbed with increasing Li content, but two equal shorter ones vary between 2.341(5) and 2.372(3) Å for the two end members of $Li_xMo_2SbS_2$. In view of structurally related compounds, such as $MoSb_2S$ and β-$MoTe_2$, we find similar Mo−S contacts (∼2.38 Å) for the former, whereas for the less electronegative Te bonding, we find longer metal−chalcogen bonds (∼2.70 Å). We note that the lattice accommodates the extra strain due to the Li insertion by widening the associated bond angles within layers and chains (Figure 4b).

The effect on the nearest-neighbor (nn) Mo(1)−Mo(1) bonds inside the layers and those of the Mo(2)−Mo(2) bonds inside the chains is shown in Figure 4c. The nn intralayer Mo(1)−Mo(1) bond distance increases smoothly from 2.768(3) to 2.802(2) Å in order of increasing Li content. Similarly, the nn intrachain Mo(2)−Mo(2) bonds vary between 2.748(2) and 2.813(2) Å. These are, on average, shorter than the Mo−Mo contacts in the 2D β-$MoTe_2$ (∼2.90 Å) but of similar length in the 3D $MoSb_2S$ (∼2.77 Å). The next nearest-neighbor (nnn) Mo−Mo contacts appear to increase from 3.18412(8) to 3.18518(8) Å and are of the same length for either type of structural building block, namely, layers or chains. However, they display an unusual nonmonotonic behavior, with a crossover from negative to positive expansion at a Li content of $x \approx 0.2$, effectively mapping out the *b* axis composition evolution (inset Figure 3). This feature implies an interplay between size and electronic effects as the amount of intercalated Li increases. The elongation of the intralayer nn Sb−Sb distances (Table 2) down the *b* axis also mirrors the previous changes. In $Li_xMo_2SbS_2$, although the nn intralayer and intrachain Mo−Mo distances are somewhat longer (∼7−10%), they do not differ significantly from the intracluster bonds observed in other ternary Mo−chalcogenides, such as the $LiMo_3X_3$[24] compounds composed of linear chains of $(Mo_3X_3)^1_\infty$ clusters or the closely related Chevrel phases $Pb_xMo_6X_{8-y}$.[25] Concerning the Li coordination, we note that its nn form a distorted octahedron of LiS_5Sb type whose volume increases as the lattice swells with an increasing amount of intercalated Li cations.

4.3. Electronic Structure Calculations. The CASTEP code was utilized to calculate the electronic structure of the titled materials. We predicted the periodic structures of Mo_2SbS_2 and $LiMo_2SbS_2$, having adopted as a starting model the experimentally determined crystallographic parameters derived from the Rietveld analysis of the low-*T* NPD data of Mo_2SbS_2 and $Li_{0.31}Mo_2SbS_2$, respectively. For Mo_2SbS_2, the relative difference between theoretical and experimental lattice constants is less than 1%, whereas that for bond lengths is less than 0.5%. Electronic structure calculations were then undertaken for the predicted equilibrium structures of Mo_2SbS_2 and $LiMo_2SbS_2$ (see Tables S1 and S2 in the Supporting Information). The small discrepancies of the Mo_2SbS_2 structural models (experiment and theory) do not produce significant differences in the calculated DOS. This

(23) Castellanos, M.; West, A. R. *J. Chem. Soc., Faraday Trans.* **1980**, *76*, 2159.

(24) Dronskowski, R.; Hoffmann, R. *Inorg. Chem.* **1992**, *31*, 3107.

(25) Marezio, M.; Dernier, P. D.; Remeika, J. P.; Corenzwit, E.; Matthias, B. T. *Mater. Res. Bull.* **1973**, *8*, 657.

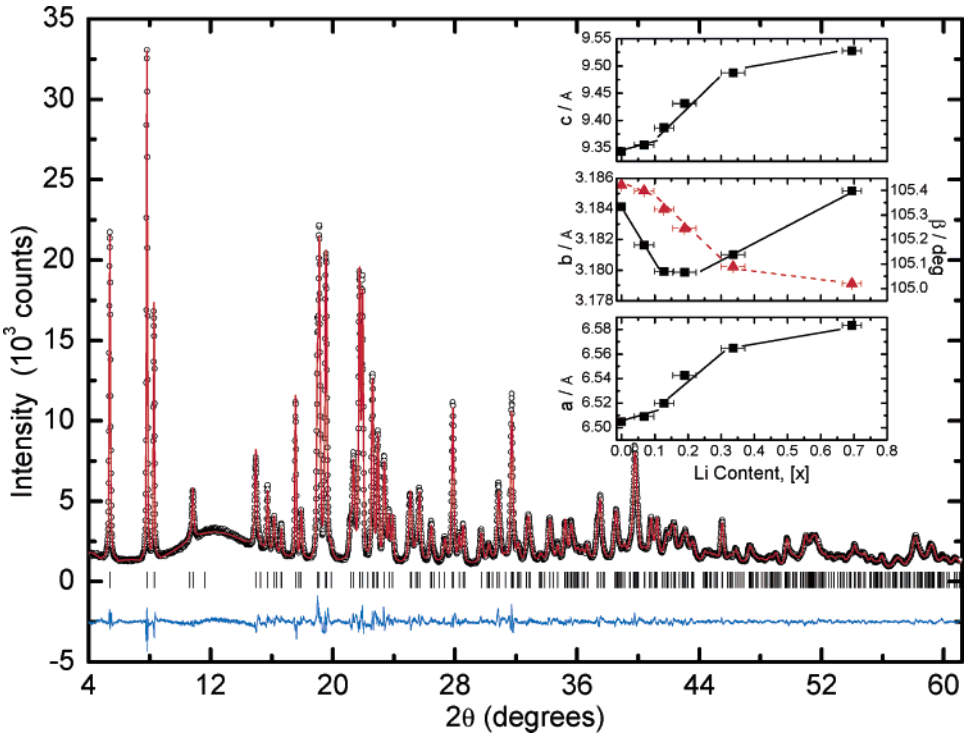

Figure 3. Observed (points) and calculated (full curve) synchrotron X-ray powder diffraction profiles from Rietveld refinement of the highest Li content derivative $Li_{0.69(3)}Mo_2SbS_2$. The reflection markers and the difference profile are shown. Inset: Monoclinic cell constants versus the refined Li content, *x*, as determined by means of the Rietveld analysis technique; the lines over the data are a guide for the eye.

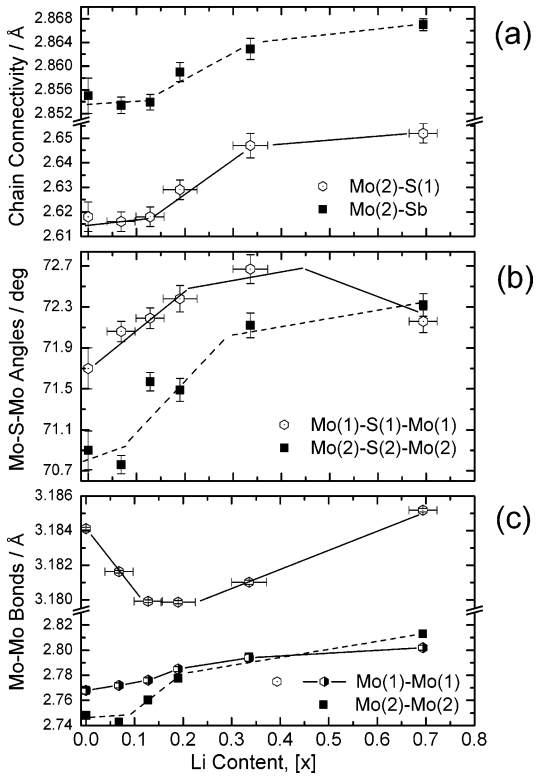

Figure 4. Composition evolution of (a) the Mo(2)−S(1) and Mo(2)−Sb bonds connecting the $[MoS]_\infty$ chainlike motifs to the $[MoSbS]_\infty$ layers, (b) the bond angles Mo(1)−$_s$(1)−Mo(1) and Mo(2)−$_s$(2)−Mo(2) defining the layers and chains, (c) the Mo(1)−Mo(1) and Mo(2)−Mo(2) bonds inside each such building unit; the lines are a guide for the eye.

is especially promising in view of the calculations for the fully lithiated derivative, $LiMo_2SbS_2$, for which there is currently no experimentally determined chemical structure. This test also provides confidence for the accuracy of the predicted electronic structures for materials with compositions between the two end members of the $Li_xMo_2SbS_2$ solid solution (see Appendix IIb in the Supporting Information).

The DOS plots for the fully optimized Mo_2SbS_2 and the $LiMo_2SbS_2$ structures, shown in Figure 5, contain the total and the projected densities arising from the s, p, and d orbital contributions for all the elements in the compounds. The results of the present DFT-GGA work for Mo_2SbS_2 are in agreement with the earlier report[13] based on a tight-binding LMTO calculation. Our work suggests that the Mo_2SbS_2 band structure (Figure 5) involves dispersive bands that cross the Fermi level (E_F), therefore indicative of a metallic electronic structure. Flat bands also cross the E_F along particular reciprocal lattice directions, for example, those defined in the range of Γ and Δ points of the Brillouin zone. In Mo_2SbS_2, the Fermi level (E_F = 4.34 eV) falls off a maximum in the DOS, hinting at subtle electronic instabilities, suggested before to be of van Hove singularity.[13]

Electron doping of the host, via Li intercalation, raised the E_F by +0.93 eV and placed it on a maximum in the DOS with $N(E_F) \cong 4.15$ electrons/eV per unit cell for $LiMo_2SbS_2$ (cf. 3.43 electrons/eV per unit cell for the parent). In the vicinity of E_F the qualitative features of the band structure do not deviate significantly from those in the parent host, with flat bands now shifted between Z and B points of the Brillouin zone. The DOS upon alloying with Li, is shifted because of the enlargement of the unit cell. The evolution of DOS around the Fermi level for various Li *x* compositions is depicted in Figure S1a (Appendix IIb, Supporting Information).

The "lower DOS region" is located between about −10 and −3.5 eV and further divided into two sub-bands (Figure 5). The partial DOS for the lower of those two sub-bands

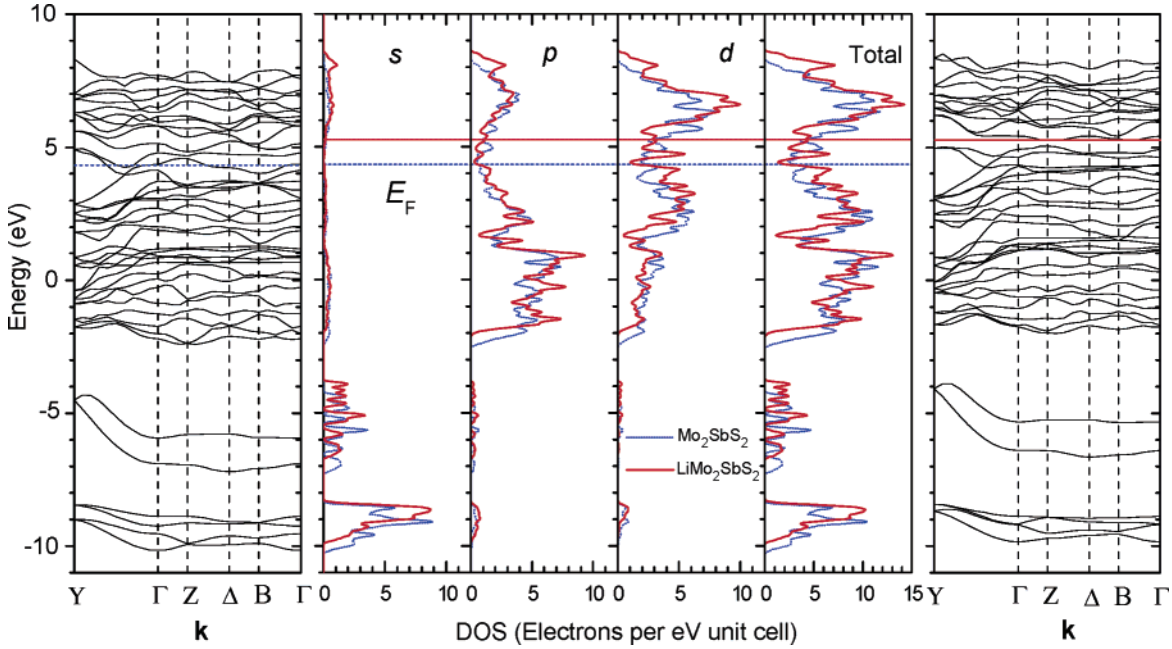

Figure 5. Band structures of Mo_2SbS_2 (left panel) and its fully lithiated derivative, $LiMo_2SbS_2$ (right panel). The middle panel compares the total density of states (DOS) for the optimized structures, whereas the projected densities arising from the s, p, and d orbital contributions for all the elements in the compounds are also shown. The Fermi energy, E_F, is drawn across the panel as a continuous dashed line.

indicates mainly S states of 3s orbitals, with a minor contribution from the 5s states of Sb, whereas for the higher sub-band, the main contribution is from the 5s orbitals of Sb. Both the p and d orbital contributions to the lower region address less than about 17% of the total DOS. Examining the modification of the electron counts upon lithiation we find the s, p, and d orbital contribution to the total DOS unaffected for the higher sub-band, but with important changes for the lower sub-band. In the latter, a decrease in the s and d contributions and enhancement of the number of p orbital electrons is effective, postulating that Li interacts mainly with the S rather than the Sb in the LiS_5Sb polyhedron. Furthermore, the "higher DOS region" (where the Fermi level falls in) is between approximately −2.5 and 8.5 eV (Figure 5). At its lower part, the partial DOS calculation suggests mainly 3p orbitals of S, but that of the 4d orbitals of Mo is also significant; a minor contribution comes from the 5p orbitals of Sb. For higher energies close to the E_F, the main character is that of the 4d orbitals of Mo, with a minor contribution from the 3p states of S. It is worth noting that the s orbital's contribution to the higher region is practically negligible and that, at the E_F, their contribution for any lithiated composition is of the order of 1.5−3%, whereas that of the p orbitals is on the order of 15−25%. This indicates that charge carriers could be mainly due to the p orbitals of S and possibly the d orbitals of Mo that effectively contribute to the E_F.

4.4. Electron Charge-Transfer Considerations. Each Li atom [$1s^2 2s$] introduced in the host structure acts on the Mo_2SbS_2 as an electron donor. In the ideal case, it could fill in the highest unoccupied bands by injecting the lattice with 2 additional electrons per unit cell of $LiMo_2SbS_2$ ($Z = 2$). To evaluate the effect of charge transfer upon intercalation, we have calculated the per formula unit Mulliken[26] populations, η, of the occupied atomic orbitals (see Table S4 in the Supporting Information). We find that only $\delta \approx 0.53$ electrons per Li are donated and distributed in the bands of the host; the effect is a partially depleted $Li^{\delta+}$ site in the $LiMo_2SbS_2$ structure. Furthermore, size changes of the unit cell play a limited role in modifying the $Li_xMo_2SbS_2$ DOS. Despite the electron redistribution that takes place in the inner part of the valence band, a major effect of the Li insertion is the filling of the d holes, which appear close to the Fermi level region (see Appendix IV in the Supporting Information).

When one assumes formal valences of −3 for Sb and −2 for S, the molybdenum must reach a mixed valency character for charge neutrality in the $Li_xMo_2SbS_2$ ($x < 1$) compound. It has been claimed before, however, that Mo_2SbS_2 is a mixed valency compound, as the Mo(1) and Mo(2) sites due to their different coordinating environments can afford accommodating distinct Mo^{3+} and Mo^{4+} oxidation states, respectively.[15] With the intercalation of Li, the estimated integrated occupation of atomic states (see Table S4 in the Supporting Information) suggests that the aforementioned nominal oxidation states are not substantially affected. That is to say formally, the 2 electrons per unit cell from each added Li atom result in a partial charge transfer, δ'/δ'', which is shared between Mo(1)-4d ($\delta' \approx -0.43$ electrons) and Mo(2)-4*d* ($\delta'' \approx -0.30$ electrons) lattice positions. In this picture, electrons are assumed not to be delocalized between molybdenums, and as such, the two different environments keep a charge disproportionation in the intercalated $Li_x(Mo^{3+\delta'}/Mo^{4+\delta''})_2SbS_2$ compound.

4.5. Transport Mechanisms. The bulk electronic properties of the Mo_2SbS_2 host and their modification by intercala-

(26) Mulliken, R. S. *J. Chem. Phys.* **1955**, *23*, 1833.

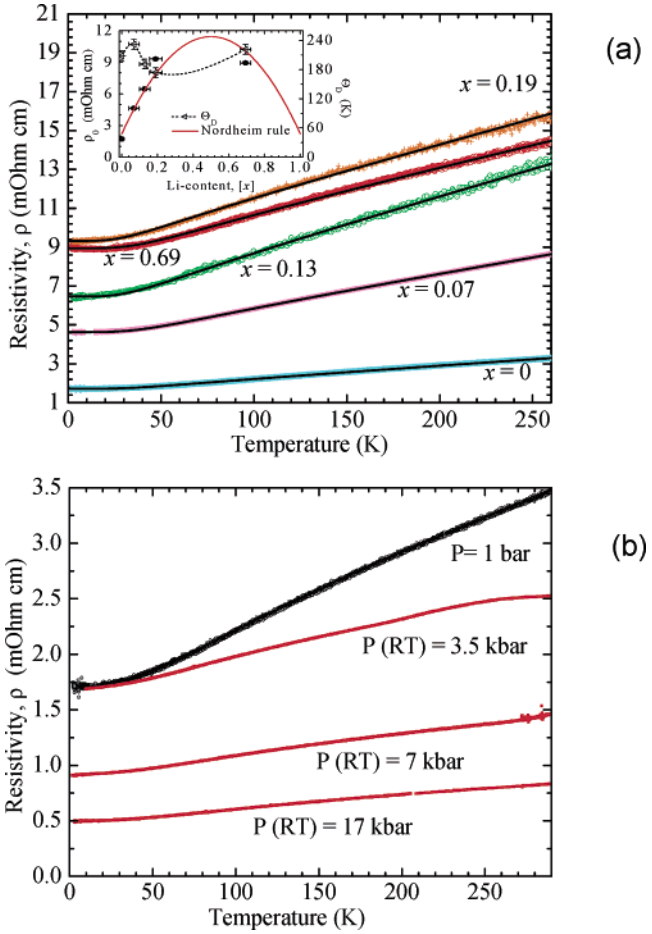

Figure 6. The temperature dependence of (a) the ambient pressure resistivity for various $Li_xMo_2SbS_2$ ($0 \leq x < 0.7$) materials; the line over the data points is a fit with the Bloch−Gruneisen function; and (b) the resistivity for the Mo_2SbS_2 host under various externally applied pressures; *P*(RT) stands for the room-temperature measurement of the hydrostatic pressure magnitude.

tion are of fundamental interest. SQUID magnetometry of the host (inset Figure 1a) has shown Pauli paramagnetism ($\chi_{TIP} = 8.51 \times 10^{-5}$ emu/mol); data were corrected for core diamagnetism (approximately -1.34×10^{-6} emu/mol) and a small Curie-tail term ($T < 15$ K, $C = 5 \times 10^{-4}$ emu K/mol). On the basis of Matthiessen's rule,[27] we have separated two electrical resistivity contributions, $\rho(T) = \rho_0 + \rho_{pure}(T)$. The residual term, ρ_0, is due to impurities or alloying effects and the thermal part, $\rho_{pure}(T)$, caused by scattering of current carriers, is due to more than one independent mechanisms. Nonlinear least-square fit of the $Li_xMo_2SbS_2$ $\rho(T)$ data (Figure 6a) was then carried out with the expression

$$\rho(T) = \rho_0 + \rho_1\left(\frac{T}{\Theta_D}\right)^5 \int_0^{\Theta_D/T} \frac{z^5 dz}{(e^z - 1)(1 - e^{-z})} + \rho_2 T^2 + \rho_3 T^3 \quad (1)$$

The second term, the Bloch−Gruneisen function (Θ_D is the Debye temperature of the metal, $z = \hbar\omega/k_BT$), is the lattice contribution arising from the scattering of the conduction electrons by thermally excited vibrations. It results in linear dependence of resisitivity at $T > \Theta_D$ and a T^5 behavior at $T \ll \Theta_D$. Because $Li_xMo_2SbS_2$ contains no magnetic elements, the T^3 term is not further justified, in addition to the T^2 term due to electron−electron scattering as the nonlinear least-square fit finds negligible probablity. From eq 1, we determined ρ_0, ρ_1, and Θ_D (Table 3). The Nordheim rule for solid solution behavior describes quantitatively the structural disorder produced by substitutional Li atoms and gives rise to $\rho_0(T \rightarrow 0) \propto x(1 - x)$ dependence (inset Figure 6a).

4.6. Electron−Phonon Coupling. It is noteworthy that the resistivity at high temperatures obeys a $\rho(T) - \rho_0 = cT$ law, with a fitted slope of $c = \rho_1/4\Theta_D$ (Table 3). Expressing ρ_1 given by the Bloch−Gruneisen equation[28] on the basis of the one-electron band theory model[27] affords a modified formula

$$\rho(T) - \rho_0 = \left(6\pi \frac{1}{e^2\hbar} \frac{\lambda_t k_B}{U_F^2 N_{FV}}\right) T \quad (2)$$

The slope is given as a function of electron−phonon coupling constant, λ_t, the electron group velocity, U_F, and the magnitude of the electronic DOS per unit volume, N_{FV}. The latter two quantities were computed (Table 3) for each Li stoichiometry at the E_F via the interpolation scheme of Appendix IIb (Supporting Information). In this approximation, N_{FV} values (Table 3) were taken from the partial DOS[29] of the s and p electrons at E_F, as those from d orbitals were assumed to have negligible contribution in the conduction because of their larger effective mass. The computed $\lambda_t \approx 2.45$ for Mo_2SbS_2 is comparable to the electron−phonon enhancement in the structurally complex high-T_c Chevrel-phase Mo−chalcogenides, $M_xMo_6X_{8-y}$ (e.g., $\lambda \approx 2.5$ for rhombohedral $Pb_{0.9}Mo_6S_{7.5}$, with $T_c = 13$ K),[30,31] but deviates from that of a simple bcc Mo metal ($\lambda \approx 0.4$, with $T_c = 0.9$ K).[32]

Enhanced coupling constants are in accord with the chemical specificity of the easily polarizable chalcogen elements, a feature that in general leads to soft bonds in their compounds. The influence of the elevated hydrostatic pressure on the electronic structure was then investigated by means of transport measurements in Mo_2SbS_2 and ac susceptibility experiments for the $Li_{0.19}Mo_2SbS_2$ composition. We found no evidence for a crossover from a metal to superconductor, for experiments down to 2 K and pressure up to 17 kbar. From the electronic structure point of view, it would suggest that as the overlap at neighboring sites increases with pressure, the bands get continuously broader

(27) Singleton, J. *Band Theory and Electronic Properties of Solids*; Oxford University Press: Oxford, U.K., 2001.
(28) Allen, P. B. In *Quantum Theory of Real Materials*; Chelikowsky, J. R., Louie, S. G., Eds; Kluwer: Boston, 1996; p 247.
(29) An estimation of the partial DOS per orbital versus Li content *x* was derived by a linear interpolation between the two end-composition values, i.e., PDOS(*x*) = *x*[PDOS(1)] + (1 − *x*)[PDOS(0)].
(30) The dimensionless quantities λ and λ_t are of similar magnitude. The latter differs in that it involves the quantity $(1 - \cos\theta)$, which characterizes transport phenomena. In simple terms, it describes the change in the wave vector of a mobile electron along its initial direction of movement during a scattering process, i.e., $|\Delta k_x| = k_F(1 - \cos\theta)$, where θ is the angle between ***k***-final and ***k***-initial. In a 3D *k*-space, proper averaging over all directions is necessary. Experimentally determined values of λ_t are found to be larger than the values of λ in superconducting metals, e.g., Pb shows $\lambda_t \approx 1.79$, with $\lambda \approx 1.55$.
(31) Andersen, O. K.; Klose, W.; Nohl, H. *Phys. Rev. B* **1978**, *17*, 1209.
(32) Papaconstantopoulos, D. A.; Boyer, L. L.; Klein, B. M.; Williams, A. R.; Morruzzi, V. L.; Janak, J. F. *Phys. Rev. B* **1977**, *15*, 4221.

Table 3. Parameters Utilized in the Calculations for the Electron−Phonon Coupling Constant, λ_t, in the $Li_xMo_2SbS_2$ Solid Solution (the composition x was obtained from the Rietveld Refined structures)

x	Θ_D (K)	ρ_1 (mOhm cm)	$c = \rho_1/4\Theta_D$ (μOhm cm K^{-1})	U_F[a] ($\times 10^7$ cm/s)	N_{FV} ($\times 10^{-3}$ electrons eV^{-1} Å^{-3})	λ_t
0.000	209.3	5.26	6.29	3.99	7.59	2.45
0.068(29)	228.5	14.68	16.06	3.88	7.43	4.25
0.128(29)	180.5	19.47	26.99	3.49	7.13	7.56
0.190(35)	174.7	18.05	25.83	3.43	7.54	7.42
0.694(29)	230.3	20.43	22.17	3.27	9.37	7.18

[a] Calculated for a finite number of energy values at a $5 \times 10 \times 4$ k-grid of points.

but still remain half-filled. Thereby, the effective mass of the carriers should decrease and the conductivity rises as shown for the temperature evolution of the Mo_2SbS_2 $\rho(T)$ with high pressure ($P = 3$, 7, and 17 kbar; Figure 6b).

4.7. Partial Localization. The unusually enhanced magnitudes of λ_t (~7 at $x = 0.69$; Table 3) in the Li-doped Mo_2SbS_2 suggest that the one-electron band theory model adopted for the previous analysis is an oversimplified approach. Many body effects (e.g., electron−electron Coulomb repulsion), which are not included in the current methodology, are important for an accurate calculation.

Phenomenologically, a percolation[33] model may be appropriate in order to describe the subtle changes of $\rho(T)$ (Figure 6a) and cell size (inset Figure 3) around $x \approx 0.19$. Assuming that each Li impurity is associated with a sphere of conductivity approximately equal to the Bohr radius of the charge carriers, as the impurity concentration increases, more and more spheres overlap, forming clusters. These gradually grow larger and coalesce to form a conducting bridge across the crystal. As a result, the slope of $\rho(T)$ at $x \geq 0.19$ (Figure 6a) adopts smaller values again. But why does the slope have the opposite trend at $x < 0.19$? According to the percolation theory, this can indicate the critical Li concentration, x_c, for appearance of improved electrical conduction. Our phenomenology should then also consider a feasible mechanism pertaining to electron localization so that the evolution of $\rho(T)$ with Li is rationalized.

The charge disproportionation at the Mo(1), Mo(2) sites and the anisotropic local deformation of their S/Sb pseudo-octahedral environment are in favor of a local lattice distortion that can trap possible charge carriers in $Li_xMo_2SbS_2$. The partially depleted Li site itself, $Li^{\delta+}$ (i.e., $\delta \approx 0.53$ for $x = 1.0$), also presents a favorable environment for entrapment. The dopant's electrostatic interactions with neighboring ions are likely to favor a polaron[34] picture similar to that in bronzes (Na_xWO_3, $0 \leq x \leq 1$).[35] Because of the electron−phonon interaction, the lattice polarization moves with a mobile electron, in effect resulting in heavier charge carriers. The formation of polarons in $Li_xMo_2SbS_2$ lowers the mobility of the electrons (s and p at E_F) and causes them to have a larger effective mass (m^*). In turn, λ_t will be adjusted to lower values than those reported in Table 3. Within this model, carrier motion is intimately linked to lattice vibrations when Mo_2SbS_2 is doped with Li; heavier carriers are foreseen until a critical composition, $x_c \approx 0.19$, when percolative conductivity comes into play.

5. Conclusions

The capability of the ternary chalcogenide Mo_2SbS_2 as a host is demonstrated by successful intercalation of lithium in the one-dimensional channels of the structure. The intercalated material, $Li_xMo_2SbS_2$ ($0 \leq x < 0.7$), is the product of soft-synthesis techniques involving Li/NH_3 reducing solutions. Rietveld refinements of neutron powder diffraction data (1.5−270 K) locate the guests and verify that no structural phase transformation takes place upon intercalation. The monoclinic structure is an assembly of infinite $[MoSbS]_\infty$ layers interconnected by $[MoS]_\infty$ chains running along the b crystal axis; a nanoporous framework system is thus formed by the pillaring chains. The small increase in the lattice volume and the efficient adjustment of framework structure after the insertion of the guests are monitored by synchrotron X-ray powder diffraction (at 300 K). We demonstrate how the aforementioned structural building blocks are tuned to allow incremental control of the dense host matrix's geometrical, chemical, and electronic environment.

The performed redox reactions result in a small perturbation of the physical properties of the host matrix; metallic electronic conductivity is found for all compositions ($0 \leq x < 0.7$) studied down to 2 K. The application of high-pressure ($P \leq 17$ kbar) increases conductivity but does not promote a metal-to-superconductor transition. The obtained data were considered in conjunction with the one-electron band-theory model for the derivation of the electron−phonon coupling constant in the series (e.g., $\lambda_t \approx 2.45$ for Mo_2SbS_2). The effect of the intercalation and the associated chemical reduction of the dense host matrix material were investigated by first-principle geometry optimizations and electronic structure calculations (DFT-GGA). The basic chemical reactivity of Li is to reduce the molybdenums' crystallographically nonequivalent sites, supporting $Mo^{3+\delta'}$ and $Mo^{4+\delta''}$ ($\delta'/\delta'' < 0$) oxidation states. We find that Li is only partially depleted from its charge and the doping of Mo_2SbS_2 mainly fills in d-holes, with leftover minority charge carriers arising from p orbitals. The evolution of λ_t upon lithiation postulates that carriers become partially localized around local lattice distortions (Mo and Li sites), giving rise to a polaron formation and relatively low carrier mobility. We suggest that with increasing Li concentration, partial localization occurs till a critical composition, $x_c \approx 0.19$. Percolative conductivity then takes over, along with a subtle crossover from negative to positive expansion in the b lattice direction.

Acknowledgment. The Marie Curie Fellowship Program of the European Commission is acknowledged (Grant HPMD−

(33) (a) Last, B. J.; Thouless, D. J. *Phys. Rev. Lett.* **1971**, *27*, 1719. (b) Kirkpatrick, S. *Phys. Rev. Lett.* **1971**, *27*, 1722.
(34) Salchow, R.; Liebmann, R.; Appel, J. *J. Phys. Chem. Solids* **1983**, *44*, 245.
(35) Lightsey, P. A.; Lilienfeld, D. A.; Holocomb, D. F. *Phys. Rev. B* **1976**, *14*, 4730.

CT-2000-0050). The authors thank A. N. Andriotis for valuable discussions on electronic structure calculations and E. N. Economou for critical reading of the manuscript. This work was partially performed at the spallation neutron source SINQ, Paul Scherrer Institute, Switzerland. Access to the synchrotron radiation facilities at Daresbury Laboratory, U.K., is gratefully acknowledged. We thank Royal Institution of Great Britain for access to their computing research facilities. A.L. thanks EMPIRIKION Foundation (Athens, Greece) for partial financial support.

Supporting Information Available: The electronic property measurements setup. Technical aspects of DFT calculations. Description of a method to calculate the electronic structure for a solid solution. Details of the synchrotron X-ray Rietveld refinementsand tabulated structural parameters for the $Li_{0.69(3)}Mo_2SbS_2$ are compared to predicted equilibrium structures of $Li_xMo_2SbS_2$ ($x = 0, 1$). Table of selected bond distances and angles for all compositions studied ($0 \leq x < 0.7$) in synchrotron experiments. Table of Mulliken population analyses results and evaluation of size versus electronic effects (PDF). This material is available free of charge via the Internet at http://pubs.acs.org.

CM0622147